

# WFPC2 CTE for Extended Sources: I. Photometric Correction

---

Grogin, N. A., Lucas, R. A., Golimowski, D., Biretta, J.

August 13, 2010

---

## ABSTRACT

*We measure the effects of charge transfer efficiency (CTE) losses on resolved sources in Wide Field and Planetary Camera 2 (WFPC2) images from 1995 to 2008. We compare medium and long exposures of the Hubble Deep Field – North taken with the F606W filter at several epochs against a “truth” mosaic of the field taken with the Advanced Camera for Surveys early in that instrument’s operation. We adopt the Dolphin (2009) functional form for the CTE photometric correction and determine the optimal coefficients for extended sources on the Wide Field (WF) detectors as a function of observation date, pre-corrected source flux, background flux, and source position on the detector.*

---

## Introduction

The charge transfer efficiency (CTE) of a charge-coupled device (CCD) can be nearly perfect upon fabrication, but it degrades steadily with exposure to energetic charged particles. This degradation of CTE is most notable in CCDs that operate for extended periods outside the Earth’s atmosphere, such as those of the Hubble Space Telescope. The continuous cosmic-ray bombardment of the HST CCDs introduces lasting defects in their lattice structure, which cause “charge traps” that prevent the transfer of accumulated charge from

pixel to pixel during read-out. These charge traps their electrons on varying timescales, that can extend to dozens or more parallel-clock cycles. There is evidence that a small fraction of WFPC2 trapped charge is released on much longer timescales, resulting in ghost images in later exposures (Biretta & Mutchler 1997).

Imperfect CTE causes charge from an imaged source to be deferred into a tapering trail extending in the direction opposite the parallel read-out (“YCTE”). The charge trails also exist in the serial read-out direction (“XCTE”), but XCTE is typically a factor of 10 or more weaker than the YCTE. Sources far from the read-out amplifier, which undergo the most charge transfers during read-out, show more prominent deferred-charge trails. In extreme cases, the deferred charge can represent 30% or more of the original charge, particularly for faint sources with large Y-coordinates in low-background images. Software remediation of the charge trailing is nontrivial in the presence of detector read-noise, source Poisson noise, and crowded fields (Massey et al. 2009; Anderson & Bedin 2010).

As of 2010, the longest operational HST CCDs were those of the Wide Field and Planetary Camera 2 (WFPC2), which were in orbit from 1993 (Servicing Mission 1) until 2009 (Servicing Mission 4). Prior studies to characterize the WFPC2 CTE based their findings upon charge trails from hot-pixels (Biretta & Kozhurina-Platais 2005) or from unresolved external sources such as stars (e.g., Whitmore, Heyer, & Casertano 1999) or cosmic rays (Riess, Biretta, & Casertano 1999). A substantial portion of WFPC2 science is concerned with compact but well-resolved sources (typically distant galaxies), whose images might not be affected by CTE in the same way as unresolved sources. For example, extended sources may fill charge traps during read-out to a greater extent than unresolved sources (Riess 2000).

This report contains the first quantitative assessment of the impact of evolving WFPC2 CTE on resolved-source photometry, and it provides a formula for correcting WFPC2 extended-source photometry akin to earlier point-source corrections (e.g., Dolphin 2009). In the following sections of this report, we describe the observations and reductions, detail the photometry and the CTE-coefficient fitting, and summarize our findings along with recommendations for their usage.

## Data

Investigating the long-term variation of WFPC2 CTE for extended sources requires repeated monitoring of a high Galactic latitude field at considerable exposure depth during most of the operational life of WFPC2. The only such field meeting all these requirements is the Hubble Deep Field – North (HDF-N).

The HDF-N has been observed with WFPC2 through the F606W filter at three widely-spaced epochs: during 1995 (Program 6337; P.I. Williams), during 2000 (Program 8389; P.I. Ibata), and during 2007–8 (Program 11032; P.I. Golimowski). The last epoch includes observations with the telescope rotated by  $180^\circ$  with respect to the original HDF-N. This rotation allows sources in the WF3 field of view to be imaged at two locations symmetric about the center of the CCD. We thereby obtain additional leverage to constrain the variation of CTE with position on the detector.

Moderately deep observations of the HDF-N also have been taken with the ACS/WFC camera using the same filter (the “wide-V” F606W) employed in most of the WFPC2 monitoring epochs. These observations come primarily from the Great Observatories Origins Deep Survey (GOODS; Cycle 11 Program 9583), with follow-up visits in Cycles 12–13 for high- $z$  supernova detection (Programs 9728, 10189, and 10339) and in Cycle 14 for grism pre-imaging (Program 10530).

The HDF-N was additionally observed in a follow-up WFPC2 epoch in 1997 using the F814W filter (Program 6473; Gilliland, Nugent & Phillips 1999). These F814W observations are not as useful for constraining CTE evolution because they are relatively close in time to the original HDF-N, and because there exist no “truth image” ACS/WFC observations in F814W as is the case with F606W. For the present study, we restrict our analysis to the F606W observations. We also have opted to omit photometry from the WF4 CCD from this study, out of concern over the WF4 bias anomaly identified in 2002 (Biretta & Gonzaga 2005). We do not wish to alias low-level photometric errors caused by the WF4 anomaly into the CTE evolution term.

Because the ACS/WFC observations were mostly taken early in that instrument’s lifetime, the differential effect of CTE across those images is very small. We include a zero-point term in the CTE fitting to allow for a time-invariant offset between WFPC2 F606W and ACS F606W.

## List of Observations

Please consult the Appendix for the full lists of exposures, both ACS/WFC and WFPC2, used to create the image stacks analyzed in this study. The listed exposures have been visually inspected and found to be free from prominent cosmetic defects such as vignetted earth-shine or bright trails from satellite/debris glint.

All F606W exposures were acquired at (for WFPC2) or near (for ACS/WFC) the coordinates of the HDF-N. The exposure times vary from 300–650 sec for ACS/WFC and

700–1400 sec for WFPC2. The position angles of the WFPC2 images are identical to the first HDF-N epoch, with the exception of the 180°-rotated Epoch 2007a and Epoch 2008. For these rotated WFPC2 epochs, only the WF3 field is used (see Fig. 1). The position angles of the ACS/WFC images vary widely, as is evident from the stacked weight-map shown in Figure 2. The diverse pointing coordinates and position angles mitigate any systematic celestial-coordinate trend in low-level CTE effects across the ACS/WFC “truth” mosaic image.

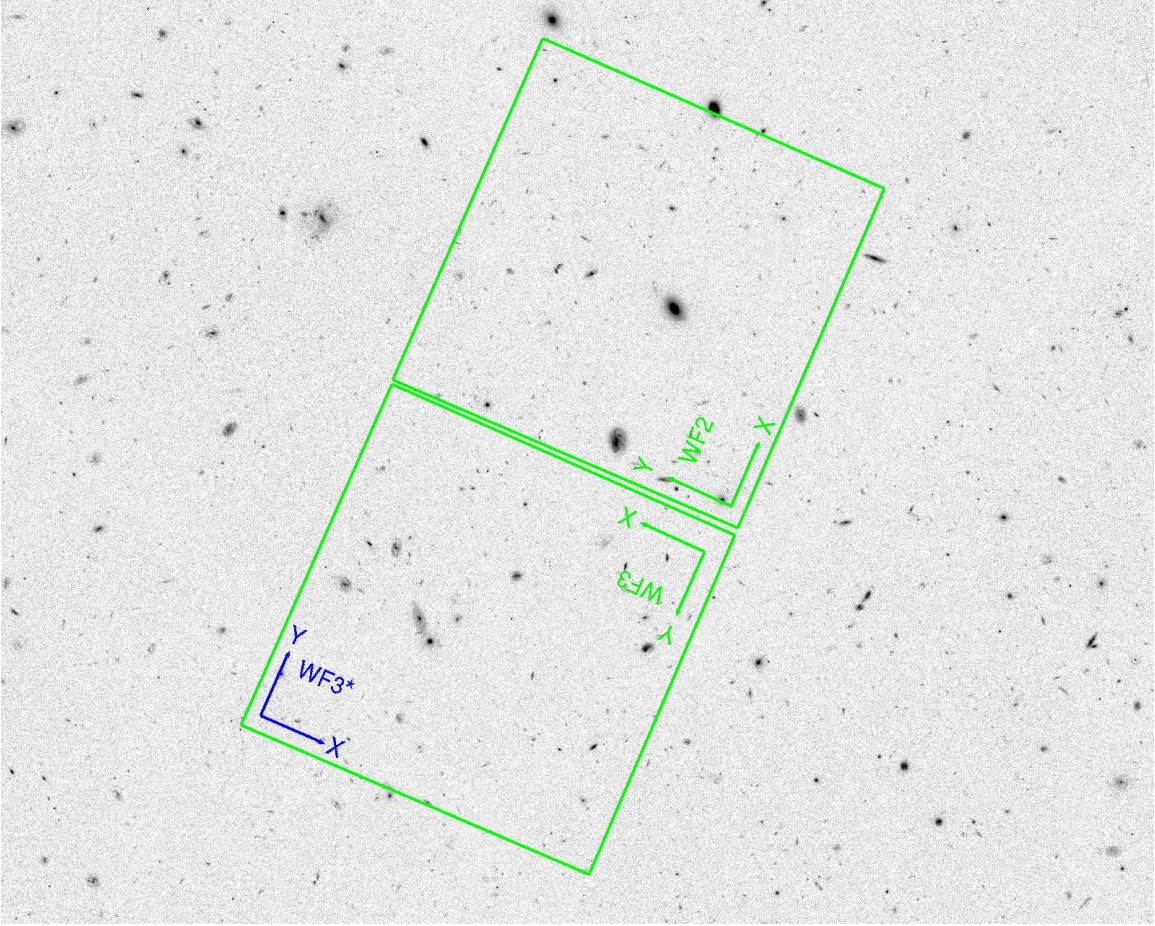


Fig. 1.— A portion of the ACS/WFC F606W “truth image” mosaic containing the WFPC2 fields investigated in this study (green boxes). The image is displayed in reverse color-map with a  $\Gamma = 0.5$  (“square root”) stretch to highlight the many faint galaxies. Green labels indicate the axis origin and orientation for the HDF-N WF2 and WF3; blue labels for the 180°-rotated epochs (denoted WF3\*).

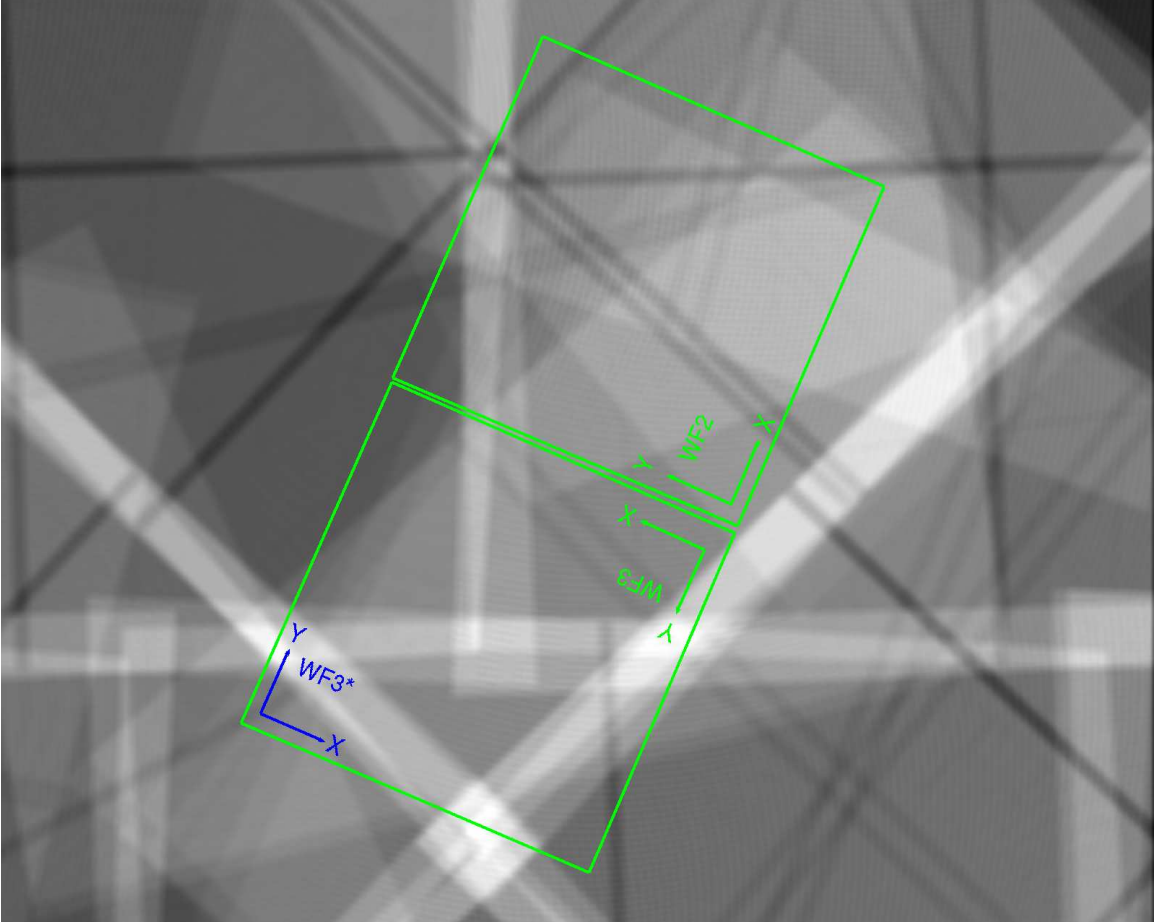


Fig. 2.— The ACS/WFC mosaic weight map corresponding to the science image of Figure 1. The ACS/WFC exposure depth within the WF2 and WF3 footprints (green boxes) varies between 8 ksec and 15 ksec, with a typical level of 11 ksec. The ACS/WFC CCD gap is imprinted on the weight map as the narrow darker bands, indicating lower exposure depth.

We created the ACS/WFC truth image using the Multidrizzle software<sup>1</sup> to stack the component images into a North-up, East-left mosaic with square  $0''.05$  pixels, very close to the native ACS/WFC pixel scale. To precisely align the component images prior to stacking, we determined delta shifts and rotation for each image by cross-correlating the drizzled single images with the GOODS-North “Version 2” mosaic. When performing this cross-correlation, we masked out the (few) stars in the GOODS mosaic. We found that the best compromise

<sup>1</sup><http://stsdas.stsci.edu/multidrizzle>

for jointly minimizing the mosaic’s pixel-noise correlation, PSF FWHM, and weight-map smoothness, was to drizzle with a square kernel at  $\text{pixfrac}=0.8$ .

## Data Characteristics

CTE losses depend upon both the fluence of the source in electrons and also the background level of the image. While the former is directly proportional to exposure time, the latter is a more complicated function of exposure time and other time-variable factors such as telescope orientation with respect to the Earth limb. Fortunately the HDF-N monitoring epochs have enough images of varying exposure time and sky background count-rate to construct multiple mosaics per epoch. We created a total of 17 WF2 and WF3 mosaics (see Appendix), each of which approximately matches the depth of our ACS/WFC truth image. Figure 3 shows the sampling in epoch (X-axis) and sky level (Y-axis).

Due to the preponderance of long broadband exposures in our study, most HDF-N image stacks have large background levels:  $\gtrsim 80e^-$ . By contrast, point-source CTE studies (e.g., Dolphin 2009) generally investigate short exposures of crowded stellar fields (typically  $\omega$  Cen) with low sky background. For example, the data-set used in the latest study by Dolphin (2009) has a median sky background of  $1.16e^-$ , and 84% of the sample has sky level  $< 9.2e^-$ . Although we are not able to probe the most extreme CTE losses that occur at the lowest background levels, it is noteworthy that most of the WFPC2 science programs concerned with photometry of compact resolved sources have been taken with moderate- to long-duration broadband exposures, whose backgrounds are much closer to  $80e^-$  than  $1e^-$ .

After segregating the WFPC2 images into bins of comparable sky level and exposure time, we used the Multidrizzle software to combine individual exposures into a higher- $S/N$  stacked image on the same world coordinate system (WCS) as the ACS/WFC truth image. We corrected the WF images’ WCS for both shift and rotation by cross-correlating single-drizzled images with the ACS/WFC truth image, after masking the latter’s stars. This full-frame image registration is not perfect, because charge-trailing causes small but systematically varying displacements of the centroids of WFPC2 sources vis-à-vis their ACS/WFC counterparts. However these CTE-induced astrometric errors are smaller for the brighter sources that dominate the cross-correlation. There is prior evidence that conclusions regarding extended-source CTE are largely insensitive to full-frame registration versus local registration on a source-by-source basis (Riess 2000).

Each WF stack comprises  $\approx 10$ – $30$  dithered images, permitting a sub-sampled drizzle to  $0''.05/\text{pixel}$  with  $\text{pixfrac}=0.6$  while avoiding unacceptable fluctuations in the mosaic weight-

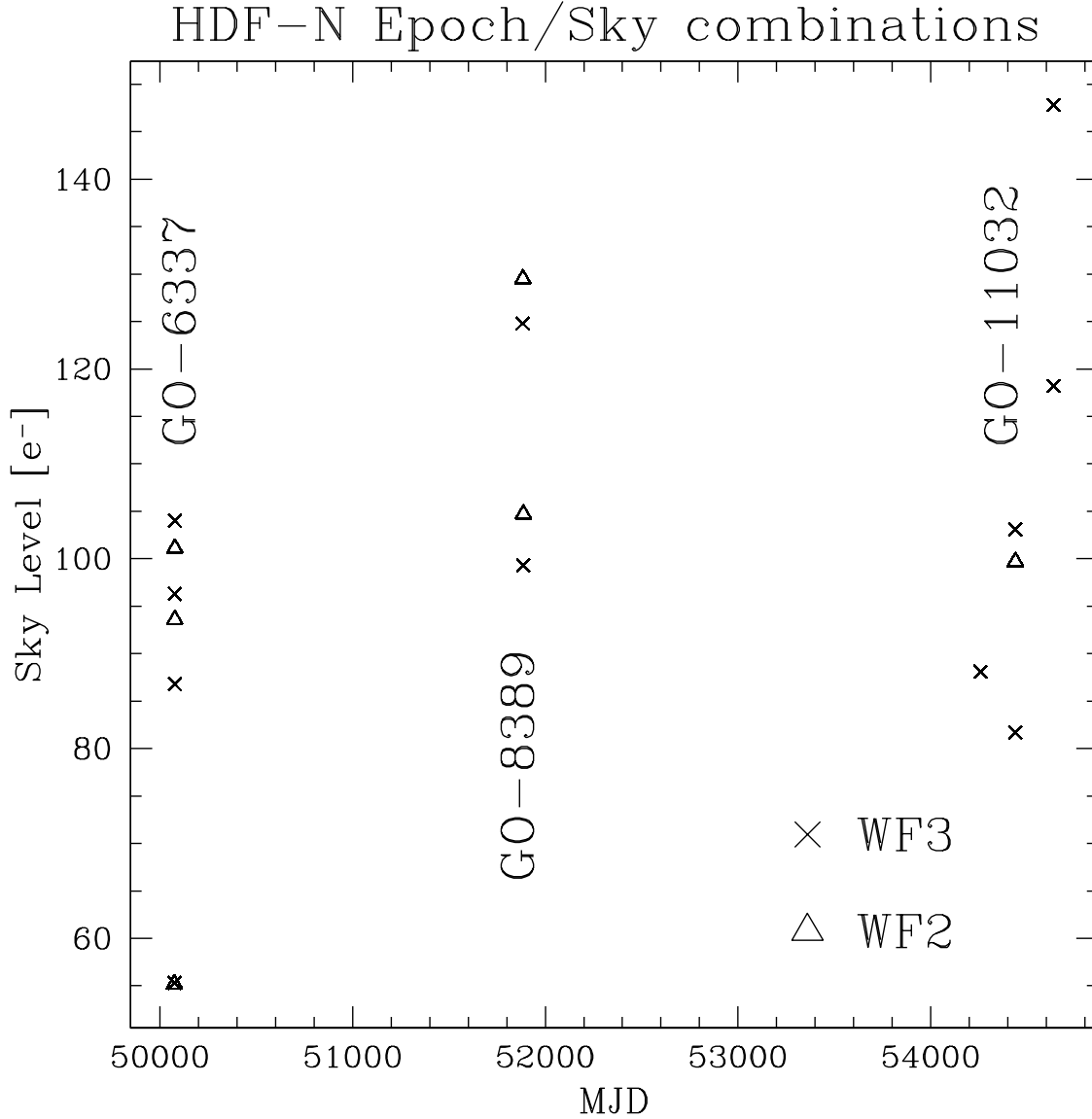


Fig. 3.— Sampling of the time domain (X-axis) and background level (Y-axis) for WFPC2 image stacks from the three HDF-N F606W monitoring campaigns used for CTE determination. The earliest observations are the original HDF-N in 1995; the last set of observations conclude in 2008. The GO-11032 observations include two epochs where the telescope was rotated  $180^\circ$  with respect to the original HDF-N, and thus only WF3 (crosses) overlapped the HDF-N. All three programs include at least one image stack of WF2 (triangles).

map. The compact dither pattern in all the HDF-N epochs insures that relative CTE losses among images of the same source in the dithered frames can be considered invariant.

## Analysis

The most straightforward approach to the extended-source photometry would be source extractions upon each image stack independently, followed by catalog-matching according to source position. Because of the diversity in sky backgrounds and mean exposure times among our image stacks, an isophote-based source extraction such as that provided by SExtractor (Bertin & Arnouts 1996) would yield inconsistent source catalogs with systematic photometry variations as a function of signal-to-noise. Such variations would rival, if not overwhelm, the CTE effects that we hope to measure.

For this reason, we instead ran SExtractor in dual-image mode, using the ACS/WFC truth image as the detection image. In this manner we determined the photometry of each WFPC2 image stack consistently from the source positions on the single detection image. No catalog-matching was required to collate the photometry for a given source in the multiple image stacks. The chief drawback to this method is that by using a fixed aperture in all images, the photometry is susceptible to systematic biases from misalignment of the image stacks and from variations in the HST focus. We later discuss the mitigation of these potential biases when fitting the CTE functional coefficients.

The input to our CTE coefficient fitting is a merged photometry catalog from all source extractions of the WF image stacks. We converted the SExtractor FLUX\_AUTO, an approximate measure of the total flux for an extended source, from the native counts/sec into both microjanskys and electrons (the latter from multiplying by the gain and by the mean exposure time in the given image stack). Because we seek to fit subtle changes in the CTE loss as a function of multiple variables, we exclude any source that does not have at least  $S/N > 5$  in *all* image stacks. The resulting merged catalog includes 5105 entries for 638 distinct sources. The distribution of source fluences and fluxes (the former is the quantity of importance to the CTE) is shown in Figure 4. The distribution of source locations across the WF2 and WF3 detectors is shown in Figure 5, plotted versus their flux differential with respect to the ACS/WFC truth image.

We adopt the functional form for CTE loss derived by Dolphin (2009) from WFPC2 images of standard star fields. We reprint the description from Dolphin’s website<sup>2</sup>, which is equivalent to the form given in Dolphin (2009), and which contains the coefficients that best-fit the unresolved sources:

Given a star brightness CTS, background level BG (both in electrons), ob-

<sup>2</sup>[http://purcell.as.arizona.edu/wfpc2\\_calib/](http://purcell.as.arizona.edu/wfpc2_calib/)

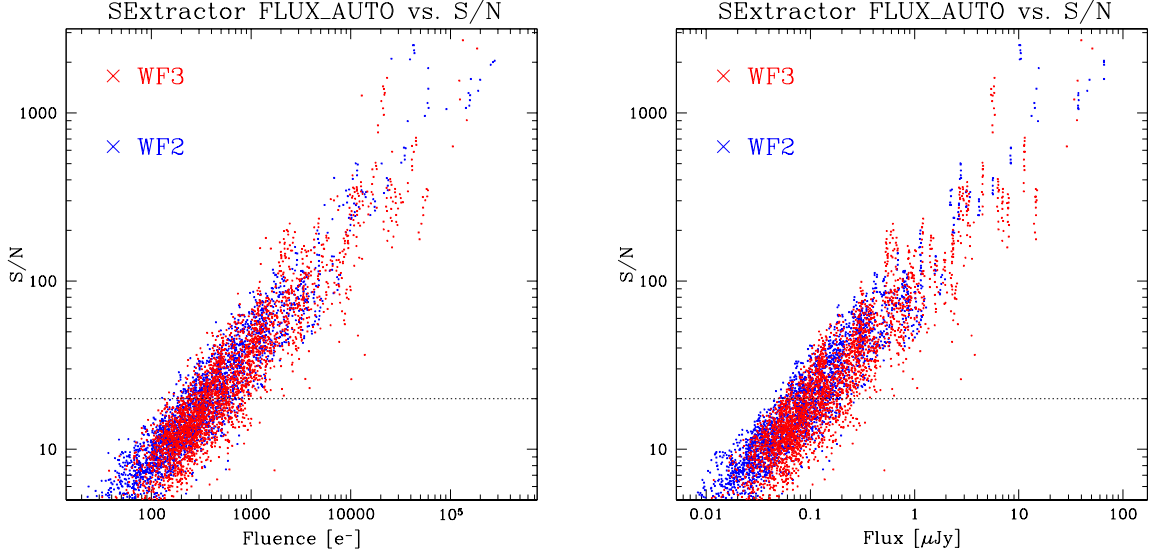


Fig. 4.— Left: *Ensemble of source fluences used in this study, extracted from the HDF-N WF2 (blue) and WF3 (red) fields, plotted against the signal-to-noise ratio as reported by SExtractor. The dotted line at  $S/N = 20$  denotes our artificial  $S/N$  ceiling for the CTE-coefficient fitting: sources with  $S/N > 20$  are treated as  $S/N = 20$  in the fitting.* Right: *As left panel, but plotted versus source flux. Photometry of the same source at different exposure times and/or backgrounds will appear as a vertical locus on this plot.*

servation date DATE (in MJD), and star position on the image  $X$  and  $Y$ , the following sequence of calculations will provide the  $XCTE$  and  $YCTE$  losses, both in magnitudes.

$$lbg = \frac{1}{2} \ln(BG^2 + 1) - 1 \quad (1)$$

$$yr = \frac{DATE - 49461.9}{365.25} \quad (2)$$

$$XCTE = 0.0077 \times \exp(-0.50 \times lbg)(1 + 0.10 \times yr) \times \frac{X}{800} \quad (3)$$

$$lct = \ln(CTS) + 0.921 \times XCTE - 7 \quad (4)$$

$$c_1 = \max(1.0 - 0.201 \times lbg + 0.039 \times lbg \times lct + 0.002 \times lct, 0.15) \quad (5)$$

$$c_2 = 0.958 \times (yr - 0.0255 \times yr^2) \times \exp(-0.450 \times lct) \quad (6)$$

$$YCTE = 2.41 \times \ln\{(1 + c_2) \times \exp[0.02239 \times c_1 \times (Y/800)] - c_2\} \quad (7)$$

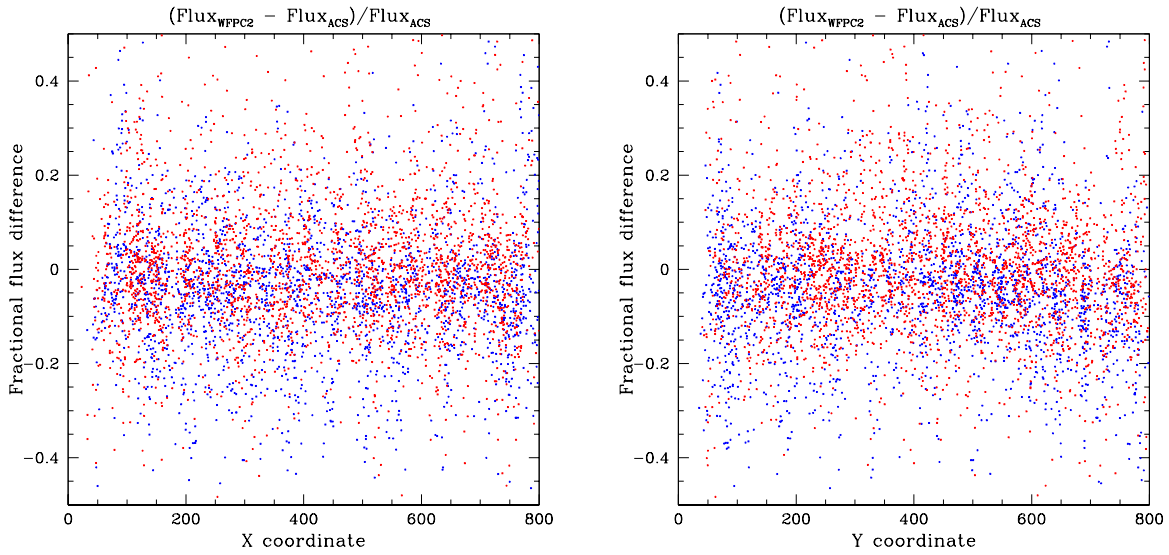


Fig. 5.— Left: *Ensemble of source X- and Y-coordinates used in this study, extracted from the HDF-N WF2 (blue) and WF3 (red) fields, plotted versus the fractional flux difference between WFPC2 and ACS flux in F606W.*

Note that the offsets of 1 for *lbg* and 7 for *lct* were put in place for numerical stability, and do not affect the solution itself.

For the resolved sources of our study, we determined the best-fit values of the thirteen free parameters of Dolphin’s prescription, plus an additional parameter for a fixed zero-point offset between WFPC2 F606W and ACS/WFC F606W — the source of our “truth image” photometry. Note that our extended-source brightnesses are determined not with Dolphin’s “HSTPhot”, but with SExtractor FLUX\_AUTO.

We performed the non-linear least-squares optimization of the Dolphin coefficients by using an IDL implementation of the downhill simplex algorithm “amoeba” from *Numerical Recipes* (Press et al. 1992). To mitigate the possibility of the algorithm reporting a local rather than global minimum of the coefficient optimization, we re-started the optimization multiple times while varying the starting positions of the optimization simplex.

To prevent the optimization from being dominated by a few bright sources, which in theory have small CTE losses, we imposed a ceiling of  $S/N = 20$  on the photometric catalog. This was accomplished by artificially increasing the SExtractor-computed error term FLUX\_ERR\_AUTO for the  $S/N > 20$  sources, such that the ratio  $FLUX\_AUTO/FLUX\_ERR\_AUTO = 20$ . We also found that the optimization was more robust if we clipped 5% of the most extreme outliers when computing the sum-of-squares at each iteration of the amoeba. This

outlier-clipping has some *a priori* motivation, insofar as photometry differences between the WF stack and the ACS/WFC truth image can arise not only from CTE and Gaussian-distributed noise, but also from non-Gaussian-distributed systematics including misalignment, focus variation, imperfect cosmic-ray rejection, possible WFPC2 first-frame anomaly (McMaster & Biretta 2010), etc.

Using the CTE coefficient values of Dolphin (2009) to correct our WF2 and WF3 photometry (with our FLUX\_AUTO as proxy for HSTPhot aperture counts), we measure the  $\chi^2$  per degree of freedom (hereafter  $\bar{\chi}^2$ ) to be 1.71. If we use the Dolphin (2009) values but optimize for a zero-point offset between WFPC2 and ACS/WFC photometry, we obtain a  $\bar{\chi}^2 = 1.66$  with a best-fit offset of  $-0.0216$  (in magnitudes, with the sense  $ZP_{WFPC2} - ZP_{ACS}$ ). When optimizing *all* the Dolphin coefficient values, as well as the zero-point term, we achieve  $\bar{\chi}^2 = 1.53$  with a negligible zero-point term of  $-0.00021$  mag. By comparison, the uncertainty in WFPC2 zero-points bracketing F606W is  $\approx 0.017$  mag (Heyer et al. 2004). Although the differences in the above  $\bar{\chi}^2$  values appear modest, they are highly significant on account of our rich data-set with  $> 4830$  degrees of freedom in the optimizations.

Table 1 lists the best-fit CTE coefficient values for the cases of resolved sources (this study) and unresolved sources (Dolphin 2009). For convenience, we also note the particular equation of the Dolphin prescription in which each coefficient appears. All coefficients are positive-valued by construction, though some appear with a leading negative sign in the Dolphin equations above.

To visualize the dependence of CTE losses on the various observables, and to compare the point-source and extended-source CTE prescriptions, we consider a “worst-case” source that is faint ( $FLUX\_AUTO = 100e^-$ ), situated far from the read-out amplifier ( $Y = 700$ ), observed late in the WFPC2 era (3 February 2008), and toward the low end of our sky-background range ( $80e^-$ ). Our predicted CTE loss for this source is  $\approx 0.14$  mag, compared with  $\approx 0.18$  mag using the Dolphin (2009) coefficient values.

The four panels of Figure 6 show the variation of the CTE for this “worst case” source as each observable is varied while the others are held at their canonical values. In each panel, the dotted line denotes the source, the green curve is the best-fit CTE prediction, and the blue curve is the Dolphin (2009) prediction. As is evident in the top two panels showing the CTE dependence on source fluence and sky background, our data-set of long-exposure broadband photometry inhabits a region in the observables space that causes jagged CTE curves when using the Dolphin (2009) coefficient values (blue curves). For most of the observables, our computed CTE losses are below those of Dolphin across virtually the whole range of variation, sometimes by more than 0.1 mag.

Resolved <sup>a</sup>	Unresolved <sup>b</sup>	Eqn.
49478.1	49461.9	2
0.4690	0.0077	3
2.20	0.50	3
2.88	0.10	3
0.0594	0.201	5
1.080	0.039	5
0.684	0.002	5
0.022	0.15	5
$4.82 \times 10^{-5}$	0.958	6
0.0603	0.0255	6
0.673	0.450	6
$1.00 \times 10^{-4}$	2.41	7
0.1288	0.02239	7

Table 1: *CTE Formula Coefficients for Resolved and Unresolved Sources*

<sup>a</sup>This study.

<sup>b</sup>Dolphin (2009)

The exception is our best-fit variation of CTE losses with epoch, shown in the lower-right panel of Figure 6. In this case, the Dolphin coefficient values produce the aesthetically superior CTE curve, with only a minor quadratic component. This quadratic term in the time evolution, introduced subsequent to the Dolphin (2000) study, has been abused by our data-set to produce an unrealistic *inflection* of the CTE loss near MJD=52500. Continual exposure to cosmic rays should continually worsen the WFPC2 CTE. There have been no changes to the operating parameters of the WFPC2 CCDs (temperature, etc.) that would explain a lessening of CTE magnitude between our Epoch 2000 data (MJD $\approx$ 51900) and our Epoch 2007–8 data (MJD $\approx$ 54500). We suspect this prominent quadratic term is due to the sparse sampling of our data in the time domain — effectively only three points (see Figure 3) to constrain a quadratic dependence.

Because our latest HDF-N monitoring epoch is near the end of the WFPC2 operational lifetime, and thus the time-extrapolation of the CTE curve will never be large, we do not

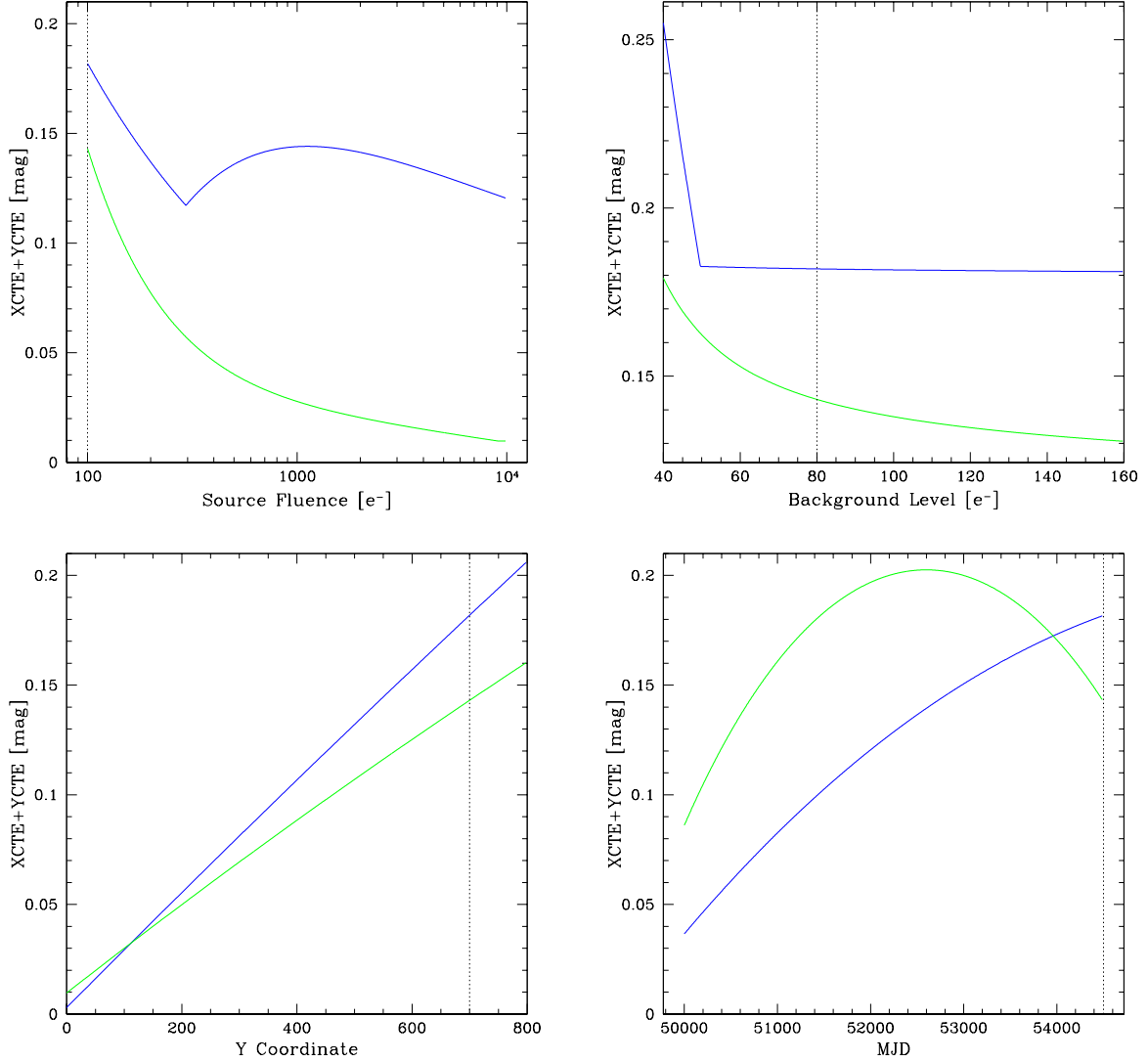


Fig. 6.— *Best-fit variation of extended-source CTE losses (Y-axis) versus source fluence (top left), background level (top right), source Y-coordinate on the WF detector (lower left), and date of observation (lower right). The dotted line in each panel shows the CTE loss for a base-line source with  $FLUX\_AUTO = 100e^-$  located at  $Y=700$  with an  $80e^-$  background, observed on  $MJD=54500$  (3 February 2008). Green shows the full coefficient optimization; blue shows the Dolphin (2009) unresolved-source CTE coefficients with optimization only for the ACS-WFPC2 F606W zero-point offset.*

consider the time-domain CTE inflection of our best-fit coefficient values to present a crisis of confidence.

## Summary and Discussion

We have analyzed multiple epochs of HDF-N imaging with WFPC2 to derive CTE coefficients suitable for correcting the measured fluxes of localized extended sources against a moderate to high background level. This represents the first quantification of extended-source CTE losses for WFPC2 photometry, following upon the study by Riess (2000) of CTE-induced distortions to WFPC2 galaxy surface-brightness profiles. We recommend the use of our best-fit CTE coefficients (Table 1) to correct WFPC2 extended-source photometry, at least in the regime of moderate- to high-background level, in preference to the Dolphin (2009) coefficient values derived for point-source CTE.

We are currently completing a parallel study on WFPC2 CTE-induced morphological distortion in these HDF-N images, as quantified by the galaxy concentration and asymmetry parameters (Conselice 2003). The importance of CTE correction to galaxy morphology, particularly as regards weak-lensing studies, has received recent attention in ACS/WFC imagery (Rhodes et al. 2010).

Although correcting for CTE photometry losses *post hoc* at the source level has been the focus of this study and most previous CTE studies, there has been recent ferment in developing software algorithms to back out the CTE charge-trailing at the pixel level, prior to photometric (or morphological) measurement (Massey et al. 2009; Anderson & Bedin 2010). If pixel de-trailing can be perfected, and without significantly worsening the noise properties of the de-trailed image, this approach should in principle be superior to a *post hoc* CTE correction derived from a statistical ensemble of sources with imperfect sampling of the dependent variables. While the current efforts are focused upon ACS/WFC correction, their success would bode well for a pixel-based CTE correction to the WFPC2 archive.

## Acknowledgments

We express our gratitude to the HST Telescope Time Review Board for granting additional HST orbits to the HDF-N monitoring program 11032, allowing us to repeat exposures corrupted by earth-shine. We thank R. Gilliland, W. Hack, and A. Koekemoer for helpful discussions regarding the Multidrizzling (and co-aligning) of our WFPC2 and ACS imagery.

## References

- Anderson, J. & Bedin, L. 2010, PASP, submitted
- Bertin, E. & Arnouts, S. 1996, A&AS, 117, 393

- Biretta, J. & Gonzaga, S. 2005, *Instrument Science Report WFPC2 2005-002* (Baltimore: STScI)
- Biretta, J. & Kozhurina-Platais, V. 2005, *Instrument Science Report WFPC2 2005-001* (Baltimore: STScI)
- Biretta, J. & Mutchler, M. 1997, *Instrument Science Report WFPC2 1997-005* (Baltimore: STScI)
- Conselice, C. J. 2003, *ApJS*, 147, 1
- Dolphin, A. E. 2000, *PASP*, **112**, 1397
- Dolphin, A. E. 2009, *PASP*, **121**, 655
- Gilliland, R. L., Nugent, P. E., & Phillips, M. M. 1999, *ApJ*, 521, 30
- Heyer, I., Richardson, M., Whitmore, B., & Lubin, L. 2004, *Instrument Science Report WFPC2 2004-001* (Baltimore: STScI)
- McMaster, M. & Biretta, J. 2010, *Instrument Science Report WFPC2 2010-001* (Baltimore: STScI)
- Massey, R., Stoughton, C., Leauthaud, A., Rhodes, J., Koekemoer, A., Ellis, R., & Shaghoul-  
lian, E. 2010, *MNRAS*, 401, 371
- Press W. H., Teukolsky S. A., Vetterling W. T., Flannery B. P. 1992, *Numerical Recipes:  
The Art of Scientific Computing* (2nd ed.; New York: Cambridge University Press)
- Rhodes, J., Leauthaud, A., Stoughton, C., Massey, R., Dawson, K., Kolbe, W., & Roe,  
N. 2010, *PASP*, 122, 439
- Riess, A. 2000, *Instrument Science Report WFPC2 2000-004* (Baltimore: STScI)
- Riess, A., Biretta, J., & Casertano, S. 1999, *Instrument Science Report WFPC2 1999-004*  
(Baltimore: STScI)
- Whitmore, B., Heyer, I., & Casertano, S. 1999, *PASP*, 111, 1559

## Appendix

### A. Specific Exposures Used in Image Stacks

In this Appendix we tabulate all exposures used to create each of the epoch and background combinations of WF2 and WF3 image stacks (see Fig. 3), as well as the exposures combined to make the the ACS “truth” image (Fig. 1). For WFPC2 these are the pipeline-processed “\_c0h.fits” files, while for ACS these are the pipeline-processed “\_flt.fits” files. For WFPC2 epochs containing more than one sky level, the exposure lists are ordered by increasing sky level.

j8dnb1bpq	j8dnb1bsq	j8dnb2dcq	j8dnb2dfq	j8dnb7gyq	j8dnb7h1q
j8dnc8uxq	j8dnc8v1q	j8dnc9f1q	j8dnc9f4q	j8dnd0g0q	j8dnd0g3q
j8dnd2j5q	j8dnd2j9q	j8dnd3kdq	j8dnd3kiq	j8dne2ssq	j8dne2t6q
j8dne3z4q	j8dne3z8q	j8dne7i3q	j8dne7i7q	j8dne8j8q	j8dne8jcq
j8dnf9vwq	j8dnf9vzq	j8dng0ojq	j8dng0omq	j8dng1qzq	j8dng1r3q
j8dng3cmq	j8dng3d0q	j8dng4ejq	j8dng4enq	j8dnh3u3q	j8dnh3u7q
j8dnh4nsq	j8dnh4nwq	j8dnh8weq	j8dnh8wiq	j8dnh9v9q	j8dnh9vdq
j8dnj2mrq	j8dnj2muq	j8n1r1dgc	j91wd2gsq	j91wd3hiq	j91wd7jmq
j91wd8laq	j91we4x7q	j91we5niq	j91we6u6q	j91we8mgq	j91we9tnq
j94sb1dsq	j94sb1duq	j94se1cuq	j94se1cwq	j9fag1qeq	j9fag2qlq
j9fag8xrq	j9fag9y5q	j9fagfh8q	j9fagghfq	j9fah1dlq	j9fah2dzq
j9fah8l9q	j9fah9urq	j9fahfgwq	j9fahgh3q		

Table 2: ACS “Truth” Exposures

u31p020at	u31p020dt	u31p020ft	u31p020gt	u31p021dt	u31p021gt
u31p030it	u31p030pt	u31p030qt	u31p0406t	u31p0407t	u31p0712t
u31p0713t	u31p0715t	u31p0803t	u31p080dt	u31p080et	u31p081dt
u31p081ft	u31p081ht	u31p081tt	u31p081vt	u31p081zt	u31p0824t
u31p0827t	u31p0829t				

Table 3: WF2; Epoch 1995 (GO-6337); Sky Level 1

u31p030kt	u31p0402t	u31p0506t	u31p0604t	u31p0606t	u31p0701t
u31p070ft	u31p070it	u31p070lt	u31p070yt	u31p0718t	u31p0719t
u31p071bt	u31p071et	u31p071it	u31p071lt	u31p071pt	u31p071st
u31p0809t	u31p080jt	u31p080kt	u31p080mt	u31p080tt	

Table 4: *WF2; Epoch 1995 (GO-6337); Sky Level 2*

u31p0404t	u31p070bt	u31p070ct	u31p070ht	u31p070mt	u31p070ot
u31p070pt	u31p0710t	u31p071ft	u31p071mt	u31p071qt	u31p071tt
u31p071vt	u31p080nt	u31p080ut	u31p080xt	u31p080zt	u31p0810t
u31p0813t	u31p0815t	u31p0818t			

Table 5: *WF2; Epoch 1995 (GO-6337); Sky Level 3*

u5ei0108r	u5ei0502r	u5ei0504r	u5ei0506r	u5ei0508r	u5ei0509r
u5ei050ar	u5ei0602r	u5ei0604r	u5ei0606r	u5ei0608r	u5ei0609r
u5ei060ar	u5ei0702r	u5ei0704r	u5ei0706r	u5ei0708r	u5ei0709r
u5ei070ar					

Table 6: *WF2; Epoch 2000 (GO-8389); Sky Level 1*

u5ei0106r	u5ei010ar	u5ei0204r	u5ei0206r	u5ei0209r	u5ei0304m
u5ei0306r	u5ei0309r	u5ei0402r	u5ei0404r	u5ei0407r	u5ei0408r
u5ei0409r	u5ei040ar	u5ei0505r	u5ei0507r	u5ei0603r	u5ei0605r
u5ei0607m	u5ei0701r	u5ei0703r	u5ei0705r	u5ei0707r	

Table 7: *WF2; Epoch 2000 (GO-8389); Sky Level 2*

u9y90901m	u9y90902m	u9y90903m	u9y90904m	u9y90905m	u9y90906m
u9y90907m	u9y90908m	u9y90909m	u9y9090am	u9y91001m	u9y91002m
u9y91003m	u9y91004m	u9y91005m	u9y91006m	u9y91007m	u9y91008m

Table 8: *WF2; Epoch 2007b (GO-11032)*

u31p020at	u31p020dt	u31p020ft	u31p020gt	u31p021dt	u31p021gt
u31p030it	u31p030pt	u31p030qt	u31p0406t	u31p0407t	u31p0712t
u31p0713t	u31p0715t	u31p0803t	u31p080dt	u31p080et	u31p081dt
u31p081ft	u31p081ht	u31p081tt	u31p081vt	u31p081zt	u31p0824t
u31p0827t	u31p0829t				

Table 9: *WF3; Epoch 1995 (GO-6337); Sky Level 1*

u31p030kt	u31p0606t	u31p0701t	u31p0708t	u31p070st	u31p070yt
u31p0718t	u31p0719t	u31p071bt	u31p071et	u31p071it	u31p071lt
u31p0809t	u31p080jt	u31p080kt			

Table 10: *WF3; Epoch 1995 (GO-6337); Sky Level 2*

u31p0402t	u31p0506t	u31p0604t	u31p0709t	u31p070et	u31p070ft
u31p070ht	u31p070it	u31p070lt	u31p070mt	u31p070ot	u31p070pt
u31p071ft	u31p071pt	u31p071st	u31p071vt	u31p080mt	u31p080tt
u31p080zt					

Table 11: *WF3; Epoch 1995 (GO-6337); Sky Level 3*

u31p0404t	u31p070bt	u31p070ct	u31p0710t	u31p071jt	u31p071qt
u31p071tt	u31p071wt	u31p080nt	u31p080ut	u31p080xt	u31p0810t
u31p0812t	u31p0813t	u31p0815t	u31p0816t	u31p0818t	u31p0819t

Table 12: *WF3; Epoch 1995 (GO-6337); Sky Level 4*

u5ei0108r	u5ei020ar	u5ei0502r	u5ei0504r	u5ei0506r	u5ei0508r
u5ei0509r	u5ei050ar	u5ei0604r	u5ei0606r	u5ei0608r	u5ei0609r
u5ei060ar	u5ei0704r	u5ei0706r	u5ei0708r	u5ei0709r	u5ei070ar

Table 13: *WF3; Epoch 2000 (GO-8389); Sky Level 1*

u5ei0104r	u5ei0106r	u5ei0109r	u5ei010ar	u5ei0201r	u5ei0204r
u5ei0206r	u5ei0209r	u5ei0301r	u5ei0304m	u5ei0307r	u5ei0309r
u5ei0402r	u5ei0404r	u5ei0405r	u5ei0406r	u5ei0407r	u5ei0408r
u5ei0409r	u5ei040ar	u5ei0501r	u5ei0503r	u5ei0505r	u5ei0507r
u5ei0601r	u5ei0603r	u5ei0605r	u5ei0607m	u5ei0701r	u5ei0703r
u5ei0705r	u5ei0707r				

Table 14: *WF3; Epoch 2000 (GO-8389); Sky Level 2*

u9y91103m	u9y91104m	u9y91106m	u9y91107m	u9y91109m	u9y91201m
u9y91202m	u9y91203m	u9y91204m	u9y91205m	u9y91206m	u9y91207m
u9y91208m					

Table 15: *WF3; Epoch 2007a (GO-11032)*

u9y90901m	u9y90903m	u9y90905m	u9y90907m	u9y90909m	u9y91001m
u9y91003m	u9y91005m	u9y91007m			

Table 16: *WF3; Epoch 2007b (GO-11032); Sky Level 1*

u9y90902m	u9y90904m	u9y90906m	u9y90908m	u9y9090am	u9y91002m
u9y91004m	u9y91006m	u9y91008m			

Table 17: *WF3; Epoch 2007b (GO-11032); Sky Level 2*

u9y95102m	u9y95104m	u9y95106m	u9y95108m	u9y9510am	u9y95202m
u9y95204m	u9y95206m	u9y95208m			

Table 18: *WF3; Epoch 2008 (GO-11032); Sky Level 1*

u9y95101m	u9y95103m	u9y95105m	u9y95107m	u9y95109m	u9y95201m
u9y95203m	u9y95205m	u9y95207m			

Table 19: *WF3; Epoch 2008 (GO-11032); Sky Level 2*